The Astrophysical Journal, 933:182 (15pp), 2022 July 10 https://doi.org/10.3847/1538-4357/ac63cc

COMAP Early Science. I. Overview

Kieran A. Cleary[1], Jowita Borowska[2], Patrick C. Breysse[3], Morgan Catha[4], Dongwoo T. Chung[5,6], Sarah E. Church[7], Clive Dickinson[8], Hans Kristian Eriksen[2], Marie Kristine Foss[2], Joshua Ott Gundersen[9], Stuart E. Harper[8], Andrew I. Harris[10], Richard Hobbs[4], Håvard T. Ihle[2], Junhan Kim[1], Jonathon Kocz[1,11], James W. Lamb[4], Jonas G. S. Lunde[2], Hamsa Padmanabhan[12], Timothy J. Pearson[1], Liju Philip[13], Travis W. Powell[4], Maren Rasmussen[2], Anthony C. S. Readhead[1], Thomas J. Rennie[8], Marta B. Silva[2], Nils-Ole Stutzer[2], Bade D. Uzgil[1,14], Duncan J. Watts[2], Ingunn Kathrine Wehus[2], David P. Woody[4], Lilian Basoalto[15], J. Richard Bond[5], Delaney A. Dunne[1], Todd Gaier[13], Brandon Hensley[16], Laura C. Keating[17], Charles R. Lawrence[13], Norman Murray[5], Roberta Paladini[18], Rodrigo Reeves[15], Marco P. Viero[1], and Risa H. Wechsler[7]
(COMAP Collaboration)

[1] California Institute of Technology, 1200 E. California Blvd., Pasadena, CA 91125, USA; kcleary@astro.caltech.edu
[2] Institute of Theoretical Astrophysics, University of Oslo, P.O. Box 1029 Blindern, NO-0315 Oslo, Norway
[3] Center for Cosmology and Particle Physics, Department of Physics, New York University, 726 Broadway, New York, NY 10003, USA
[4] Owens Valley Radio Observatory, California Institute of Technology, Big Pine, CA 93513, USA
[5] Canadian Institute for Theoretical Astrophysics, University of Toronto, 60 St. George Street, Toronto, ON, M5S 3H8, Canada
[6] Dunlap Institute for Astronomy and Astrophysics, University of Toronto, 50 St. George Street, Toronto, ON, M5S 3H4, Canada
[7] Kavli Institute for Particle Astrophysics and Cosmology & Physics Department, Stanford University, Stanford, CA 94305, USA
[8] Jodrell Bank Centre for Astrophysics, Department of Physics and Astronomy, The University of Manchester, Oxford Road, Manchester, M13 9PL, UK
[9] Department of Physics, University of Miami, 1320 Campo Sano Avenue, Coral Gables, FL 33146, USA
[10] Department of Astronomy, University of Maryland, College Park, MD 20742, USA
[11] Department of Astronomy, University of California, Berkeley, CA 94720, USA
[12] Département de Physique Théorique, Université de Genève, 24 Quai Ernest-Ansermet, CH-1211 Genéve 4, Switzerland
[13] Jet Propulsion Laboratory, California Institute of Technology, 4800 Oak Grove Drive, Pasadena, CA 91109, USA
[14] National Radio Astronomy Observatory, Pete V. Domenici Array Science Center, P.O. Box 0, Socorro, NM 87801, USA
[15] CePIA, Departamento de Astronomía, Universidad de Concepción, Chile
[16] Department of Astrophysical Sciences, Princeton University, Princeton, NJ 08544, USA
[17] Infrared Processing Analysis Center, California Institute of Technology, Pasadena, CA 91125, USA
[18] Leibniz-Institut für Astrophysik Potsdam (AIP), An der Sternwarte 16, D-14482 Potsdam, Germany
Received 2021 November 19; revised 2022 February 24; accepted 2022 April 1; published 2022 July 13

Abstract

The CO Mapping Array Project (COMAP) aims to use line-intensity mapping of carbon monoxide (CO) to trace the distribution and global properties of galaxies over cosmic time, back to the Epoch of Reionization (EoR). To validate the technologies and techniques needed for this goal, a Pathfinder instrument has been constructed and fielded. Sensitive to CO(1–0) emission from $z = 2.4$–3.4 and a fainter contribution from CO(2–1) at $z = 6$–8, the Pathfinder is surveying 12 deg^2 in a 5 yr observing campaign to detect the CO signal from $z \sim 3$. Using data from the first 13 months of observing, we estimate $P_{\rm CO}(k) = -2.7 \pm 1.7 \times 10^4\ \mu{\rm K}^2\,{\rm Mpc}^3$ on scales $k = 0.051\ -0.62\ {\rm Mpc}^{-1}$, the first direct three-dimensional constraint on the clustering component of the CO(1–0) power spectrum. Based on these observations alone, we obtain a constraint on the amplitude of the clustering component (the squared mean CO line temperature bias product) of $\langle Tb\rangle^2 < 49\ \mu{\rm K}^2$, nearly an order-of-magnitude improvement on the previous best measurement. These constraints allow us to rule out two models from the literature. We forecast a detection of the power spectrum after 5 yr with signal-to-noise ratio (S/N) 9–17. Cross-correlation with an overlapping galaxy survey will yield a detection of the CO–galaxy power spectrum with S/N of 19. We are also conducting a 30 GHz survey of the Galactic plane and present a preliminary map. Looking to the future of COMAP, we examine the prospects for future phases of the experiment to detect and characterize the CO signal from the EoR.

Unified Astronomy Thesaurus concepts: CO line emission (262); Cosmological evolution (336); High-redshift galaxy clusters (2007); Molecular gas (1073); Radio astronomy (1338); Astronomical instrumentation (799)

1. Introduction

Understanding the origin and evolution of the first stars and galaxies, from the cosmic dawn to the present day, is a major challenge for astrophysics and cosmology. Current instruments such as the Atacama Large Millimeter/submillimeter Array (ALMA) and the Hubble Space Telescope (HST) are being focused on these epochs, providing detailed measurements of individual high-redshift objects. Ongoing molecular line surveys of small areas of sky (1–10 sq. arcmin) are constraining the properties of the brightest galaxies during the Epoch of Galaxy Assembly (for a review, see Carilli & Walter 2013), and planned instruments will extend the reach of such small-area surveys to the Epoch of Reionization (EoR), e.g., the next generation Very Large Array (ngVLA; Decarli et al. 2018; Walter et al. 2019), the James Webb Space Telescope (JWST; e.g., Finkelstein et al. 2017), and the Nancy Grace Roman

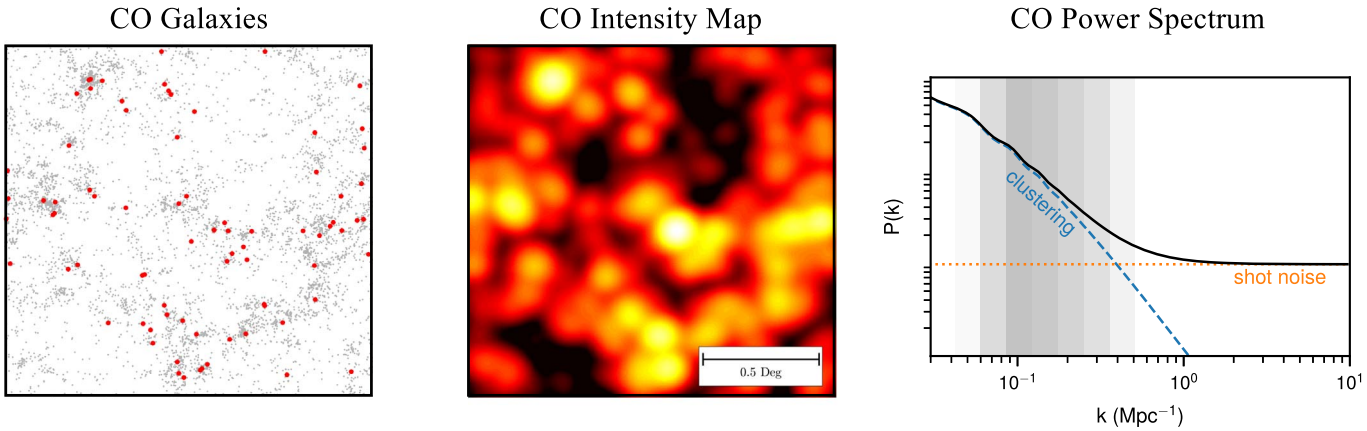

Figure 1. Left: a simulated 2.5 deg^2 field showing galaxy positions in gray (adapted from Kovetz et al. 2017). Center: simulated CO intensity map of the same field in a slice of 40 MHz bandwidth, corresponding to a redshift interval $\Delta z = 0.004$. The VLA would take about 4500 hr to cover the same area, but would detect just 1% of the galaxies (shown in red on the left). COMAP, on the other hand, is sensitive to the aggregate emission from all galaxies in the line of sight, including those too faint to detect individually. Right: a representative power spectrum for the intensity map shown in the center panel. The spectrum is composed of two components: one from the clustering of galaxies on large scales and a second that arises from the scale-independent shot noise, which dominates on small scales. The shaded region indicates schematically the scales to which the Pathfinder is most sensitive.

Space Telescope (NGRST; Akeson et al. 2019; Koekemoer et al. 2019). On the other end of the scale, measurements of the cosmic microwave background (CMB) provide a constraint on the total reionization optical depth over the largest angular scales.

What is lacking, however, is a way to bridge this huge range in spatial scales, providing constraints on the faintest galaxies that make up the bulk of the population while surveying large cosmic volumes in a reasonable time. Spectral line-intensity mapping (LIM) is an emerging technique (see Kovetz et al. 2017 for a review) that has the potential to fulfill this requirement and complement both galaxy surveys and constraints from the CMB. Unlike galaxy surveys, which trace the large-scale distribution of mass by individually detecting large numbers of galaxies, LIM measures the aggregate emission of spectral lines from unresolved galaxies and the intergalactic medium (IGM; Figure 1). The redshift of the spectral line locates the emission in the line-of-sight direction. This allows efficient mapping of the cosmic luminosity density from a variety of spectral lines over a huge volume of the universe.

Initially, most of the LIM effort has focused on 21 cm hydrogen emission from the neutral IGM, with several large experiments now underway (e.g., HERA, DeBoer et al. 2017; CHIME, Bandura et al. 2014) or planned (e.g., HIRAX, Newburgh et al. 2016; SKA, Santos et al. 2015). Interest has rapidly grown in the use of this technique to trace galaxies using redshifted 21 cm as well as the rotational carbon-monoxide (CO) transitions, the [C II] fine-structure line, and Lyα, among others.

Using CO as the tracer molecule for intensity-mapping studies is complementary to other probes and has several advantages. Many observations, starting with Brown & Vanden Bout (1991), have demonstrated that line emission from the CO transitions is bright even at high redshift. The CO emission from galaxies correlates strongly with the infrared luminosity (e.g., Carilli & Walter 2013), a proxy for star formation, providing a picture that is complementary to studies of the neutral IGM. The multiple emission lines of CO, with a well-defined frequency spacing, enable the signal to be separated from contaminating signals; this feature is not available to either H I or [C II] measurements. The levels of foreground contamination in a CO survey are substantially lower than for many other types of LIM, as CO suffers from neither the exceptionally high levels of continuum foregrounds present in 21 cm surveys nor the bright spectral line foreground present in [C II] surveys.

Purpose-built Pathfinder-scale experiments are currently pursuing detections in a variety of emission lines, including CO (COMAP,[19] the subject of this paper; AIM-CO, Kovetz et al. 2017) and [C II] (EXCLAIM, Cataldo et al. 2021; TIM, Vieira et al. 2020; TIME, Crites et al. 2014; FYST, CCAT-Prime Collaboration et al. 2021; and CONCERTO, Lagache 2018). Observations using facility instruments (e.g., ALMA and CARMA) have yielded intensity-mapping constraints on the CO shot-noise power spectrum and on the CO–galaxy cross-spectrum at redshifts in the range $1 < z < 5$ (Keating et al. 2016, 2020; Keenan et al. 2022). SPHEREx (Korngut et al. 2018), a NASA MIDEX-class mission to perform spectroscopic surveys in multiple lines, including Hα, Hβ, and Lyα, has been selected by NASA for launch in 2023.

The CO Mapping Array Project (COMAP) was funded by the United States' National Science Foundation (NSF) in 2015 to construct a pathfinding instrument for CO LIM. This Pathfinder is the first step in a long-term program that ultimately aims to trace the evolution of the global properties of galaxies, through the epoch of their assembly to cosmic reionization. Given the nascent state of the LIM field and the challenges involved in targeting the uncertain CO signal from the EoR, the goals for the Pathfinder focused on (i) constraining the CO clustering power spectrum of galaxies at $z \sim 3$, and (ii) demonstrating the technology and techniques needed for observations targeting the EoR. An ancillary science goal was to perform continuum observations of Galactic and extragalactic targets.

In this paper, the first of a series, we present an overview of early results, starting with a description of the Pathfinder instrument in Section 2. For the LIM science (Section 3), we describe the observations conducted during the Pathfinder's first LIM observing season (Section 3.2) and the LIM analysis

[19] http://comap.caltech.edu

Table 1
COMAP Early Science Papers

	Title	Reference	In This Work
I.	Overview	(this paper)	
II.	Pathfinder Instrument	Lamb et al. (2022)	Section 2
III.	CO Data Processing	Foss et al. (2022)	Section 3.3
IV.	Power spectrum methodology and results	Ihle et al. (2022)	Section 3.4
V.	Constraints and Forecasts at $z \sim 3$	Chung et al. (2022)	Sections 3.5, 3.6, 5.1
VI.	The COMAP Galactic Plane Survey	Rennie et al. (2022)	Section 4
VII.	Prospects for CO Intensity Mapping at Reionization	Breysse et al. (2022)	Section 5.2

pipeline (Section 3.3). Next, we present the power-spectrum results from this first season (Section 3.4) and discuss their implications for the global properties of galaxies at $z \sim 3$ (Section 3.5). For the continuum science, we present early results from a 30 GHz survey of the Galactic plane (Section 4). We conclude by presenting forecasts for the nominal 5 yr Pathfinder survey (Section 5.1), and prospects for the next phases of the project, targeting galaxies at $z = 5$–9 (Section 5.2). The other papers in the series (see Table 1) describe these and other aspects in significantly more detail.

2. The Pathfinder Instrument

The Pathfinder targets the 26–34 GHz frequency range, which is sensitive to the 115.27 GHz CO(1–0) line in the redshift range $z = 2.4$–3.4 and the 230.54 GHz CO(2–1) line at $z = 6$–8 (see Figure 2). The Pathfinder receiver (Figure 3) is a single-polarization 19-feed focal plane array, deployed on a 10.4 m Cassegrain telescope (Leighton 1977) at the Owens Valley Radio Observatory (OVRO), resulting in a resolution of 4.′5 at 30 GHz. There is no evidence of significant radio frequency interference in the 26–34 GHz band at OVRO. Table 2 summarizes the main instrument parameters. The first down-conversion stage, located in modules mounted on the exterior of the cryostat, shifts the 26–34 GHz RF band to a first intermediate frequency (1st IF) of 2–10 GHz. The second down-conversion stage occurs inside the telescope side-cabin, where the 2–10 GHz band from each feed is split into two 4 GHz-wide bands, each of which is quadrature down-converted to produce an "in-phase" (I) and "quadrature" (Q) signal at a 2nd IF of 0–2 GHz. Each IQ pair is input to a "ROACH-2" FPGA-based spectrometer (from a hardware design by the Center for Astronomy Signal Processing and Electronics Research, CASPER; Parsons et al. 2006). Custom FPGA code in each ROACH-2 performs separation into upper sidebands (USB) and lower sidebands (LSB), resulting in four 2 GHz-wide sidebands from each feed, each of which has 1024 spectral channels (i.e., ∼2 MHz spectral resolution). In order to process the 8 GHz bandwidth from each of the 19 feeds, 38 ROACH-2 spectrometers are needed. Spectra are recorded every 20 ms and sent via Ethernet to a storage machine in a nearby control building. From there, these data are transmitted to the Caltech campus via internet and stored on disk arrays. The spectra are then combined with pointing and housekeeping data and are available for further analysis and processing.

A "calibration vane," consisting of microwave absorber material at ambient temperature, is mounted on the side of the receiver (see Figures 3 (e) and (f)) . This vane can be moved under computer control into the path of the feed horns in order to present a blackbody at ambient temperature for determination of

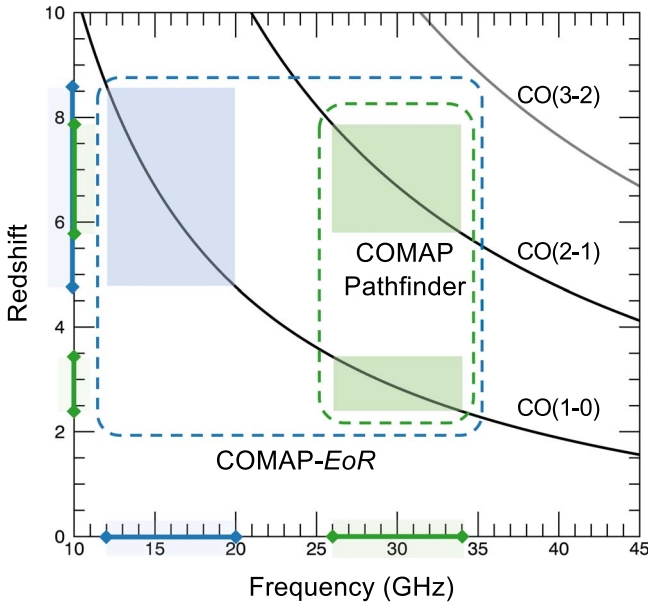

Figure 2. Redshift of the three lowest CO transition lines as a function of observed frequency. The frequency coverage for the COMAP Pathfinder Survey (26–34 GHz) is sensitive to the CO(1–0) line in the redshift range $z = 2.4$–3.4 and the CO(2–1) line at $z = 6$–8. Also shown is the frequency coverage of a future COMAP-*EoR* survey, in which a second frequency channel (12–20 GHz) is added, sensitive to the CO(1–0) line at $z = 4.8$–8.6.

Table 2
Pathfinder Instrument Parameters

Parameter	Value
Primary reflector diameter	10.4 m
No. of feeds	19
Polarization	Left-circular
Beam FWHM @ 26, 30, 34 GHz	4.9′, 4.5′, 4.4′
Beam separation on sky	12.0′ (center to center)
System temperature[a]	34–60 K (median 44 K)
Frequency resolution (native)	1.953125 MHz
Frequency resolution (science)	31.25 MHz
Frequency bands	1st IF (RF) frequency
A LSB	2–4 GHz (26–28 GHz)
A USB	4–6 GHz (28–30 GHz)
B LSB	6–8 GHz (30–32 GHz)
B USB	8–10 GHz (32–34 GHz)

Note.
[a] The range given corresponds to the central 95% of all scans between 35–65 degrees elevation, for all feeds and all sidebands (see Foss et al. 2022, Appendix A).

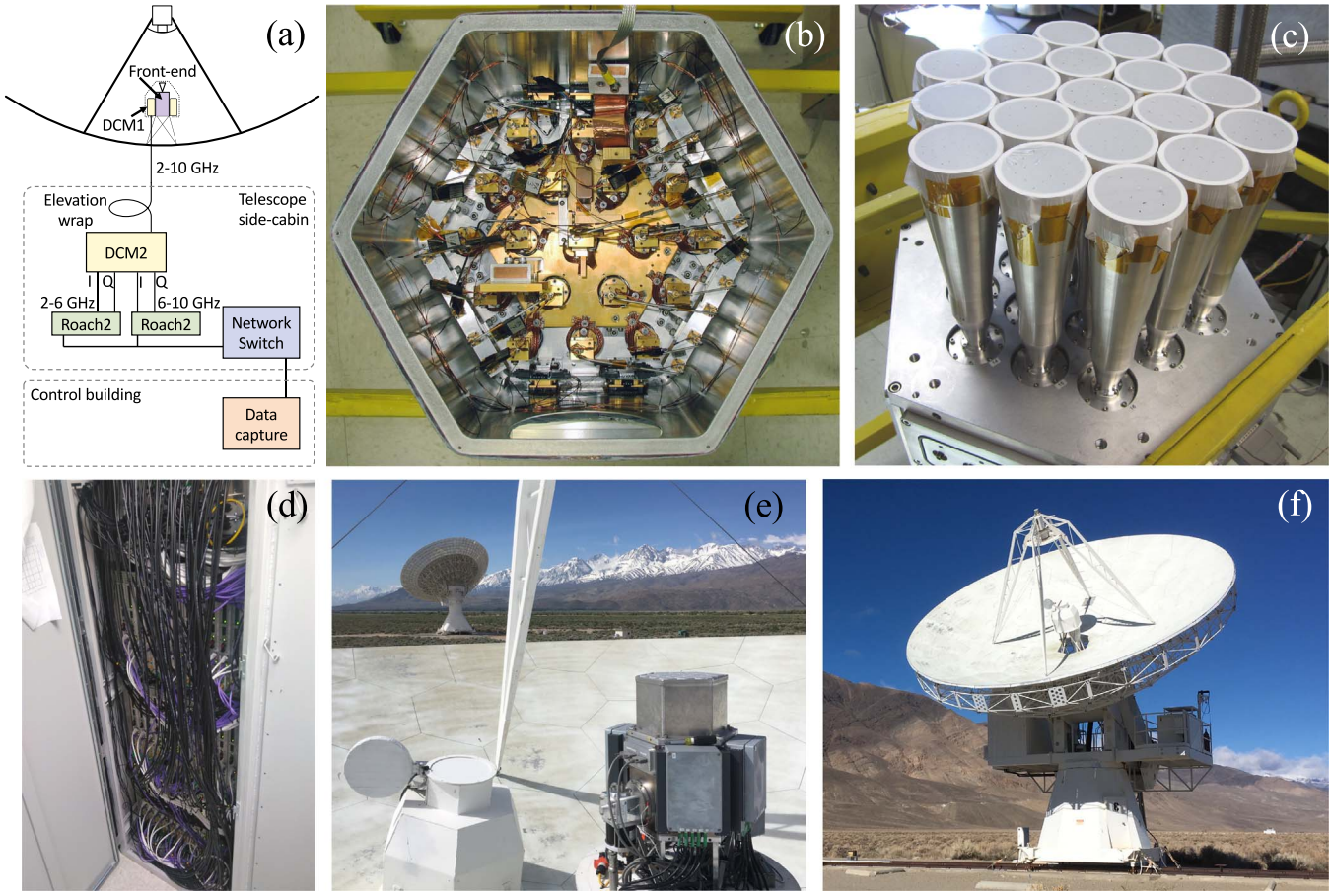

Figure 3. (a) A block diagram showing the signal path for a single feed of the 19-feed Pathfinder receiver, consisting of the cryogenic front end, first- (DCM1) and second- (DCM2) stage down-converters, ROACH-2 spectrometers, and the data storage computer. (b) Cryostat interior showing 19 low-noise amplifiers. (c) Cryostat exterior showing 19 feed horns. (d) Digital rack in telescope side-cabin with 38 ROACH-2 spectrometers. (e) Cryostat and DCM1 modules mounted at the secondary focus, with weather enclosure removed. (f) The Pathfinder receiver fielded on a 10.4 m telescope at OVRO.

the system temperature, which is used to calibrate the data to brightness temperature units.

When not in use, the vane rests at a position in the plane of the secondary supports so that it causes no additional shadowing of the aperture.

3. The Pathfinder Line Intensity Mapping Survey

3.1. Field Selection

The primary goal of the Pathfinder is to detect the power spectrum of CO(1–0) fluctuations from galaxies at $z = 2.4$–3.4 on scales relevant to clustering; that is, $\gtrsim$10 Mpc, corresponding to spatial Fourier modes, $k \lesssim 0.6\,\mathrm{Mpc}^{-1}$ (see Figure 1, right). The total detection significance (over all observable k) is predicted (in a model-dependent way) to be optimal for an individual field size $\leqslant 1$ deg^2 (Breysse et al. 2014). However, the necessity to scan the telescope (Foss et al. 2022) and the size of the feed array on the sky both impose a practical limit on how small each field can be, resulting in an effective size of around 4 deg^2. Field selection was influenced by the following considerations: (i) fields were distributed in R.A. in order to maximize observing efficiency, (ii) field locations were selected to overlap[20] with the Hobby–Eberly Telescope Dark Energy Experiment (HETDEX) galaxy survey (Hill et al. 2021; Gebhardt et al. 2021; Hill et al. 2008) in order to cross-correlate with their Lyα emitter catalog, and (iii) bright 30 GHz point sources were avoided.

The result of these considerations was a set of three ~ 4 deg^2 fields as shown in Table 3 and Figure 4. These field sizes may be further optimized in future, if a detection of the signal allows us to constrain the expected sample variance.

Table 3
COMAP Season 1 Field Location, Effective Area, and Effective Integration Time

Name	R.A. (J2000)	Decl. (J2000)	Ω_{eff} (deg^2)	τ_{eff} (hr)
Field 1	$01^{\mathrm{h}}41^{\mathrm{m}}44\overset{\mathrm{s}}{.}4$	$00°\ 00'\ 00\overset{''}{.}0$	4.24	303.7
Field 2	$11^{\mathrm{h}}20^{\mathrm{m}}00\overset{\mathrm{s}}{.}0$	$52°\ 30'\ 00\overset{''}{.}0$	3.54	346.5
Field 3	$15^{\mathrm{h}}04^{\mathrm{m}}00\overset{\mathrm{s}}{.}0$	$55°\ 00'\ 00\overset{''}{.}0$	4.00	245.9

Note. The effective area corresponds to a cutoff in the associated map's white noise level equivalent to 95% of the total integration time. The effective integration time is that assuming 100% acceptance of all 19 feeds and frequency channels.

3.2. Observations

Observations using the Pathfinder began in 2019 June and continued until 2020 August, when the receiver was removed

[20] The HETDEX field definitions changed slightly such that one of our fields lies outside their nominal survey area. However, we hope to fill in this field with additional observations.

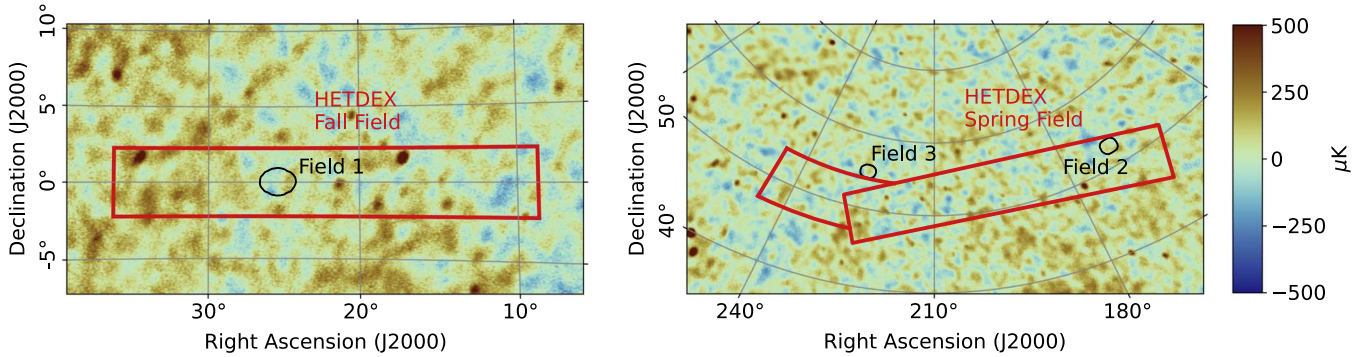

Figure 4. The three CO fields, overlaid on the Planck LFI 30 GHz full-mission map (Planck Collaboration et al. 2020). The black contours indicate the ∼4 deg^2 coverage of each field. The orange outlines correspond to the HETDEX fall (left) and spring (right) fields (Gebhardt et al. 2021).

from the telescope for maintenance. Observing resumed in 2020 November and we refer to the period before receiver maintenance as "Season 1." The LIM results presented here and in the other Early Science papers of this sequence are all based on data from Season 1 only. LIM data taken after this will be included in future publications.

Each observation of a LIM field consists of several scans, where one scan is the period between two repointings of the telescope, during which the telescope performs the same motions around a fixed point in azimuth and elevation while the target field drifts through. Two main scan patterns are used: (i) slewing in azimuth, at a fixed elevation (constant elevation scan, or "CES"), and (ii) a Lissajous pattern. Observations alternated between CES and Lissajous scan patterns on a daily basis during Season 1 (see Foss et al. 2022 for more details on these scan patterns).

During an observation, spectra were recorded every 20 ms and written to files after a period typically 1 hr in length. A measurement of the system temperature ($T_{\rm sys}$) using the calibration vane is performed at the beginning and end of this period.

Table 3 shows the effective integration time obtained on each field after pipeline filtering, for an ideal instrument with 100% acceptance of all feeds and frequency channels.

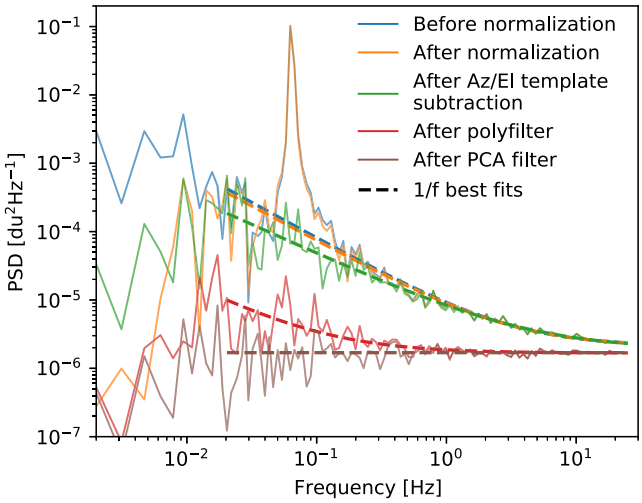

Figure 5. Power spectrum of a single scan from a 31.25 MHz band around 26.2 GHz at different stages in the analysis pipeline, with $1/f$ noise curves fitted. The power spectrum is binned with logarithmic bin sizes toward higher frequencies for clarity. Lower frequencies have been excluded from the fit, as these scales are greatly suppressed at the normalization stage. The end result of the various filters is a flat power spectrum indicating a very low level of correlated noise. See Foss et al. (2022) for details of the filters involved.

3.3. Data Analysis

Data processing starts with the raw data as recorded by the instrument, together with pointing information and housekeeping data. The first processing step is to partition each observation into individual scans, based on pointing information. The next step is to process the time-ordered data (TOD) by applying a series of filters and a time-varying gain normalization, as follows (see Figure 5 for the effect of each step).

1. The raw TOD for each frequency channel are divided by their running mean and shifted to zero-mean by subtracting 1.0 from the result. This normalization removes slow drifts and effectively flattens the instrument passband.
2. Next, contaminating signals that are correlated with pointing in the telescope frame (e.g., the "spike" shown in Figure 5 due to the scanning period of the telescope during a Lissajous scan) are removed by fitting for and removing contributions that vary with azimuth and $1/\sin(\text{elevation})$. This works well for CES scans but we have found that Lissajous-scanned data are more prone to residual ground pickup. As a result, we only include CES scans in our Season 1 analysis and observations after Season 1 only use CES scans. (The power spectra estimated for each scan type can be seen in Ihle et al. 2022.)
3. To the resulting TOD, we then perform a linear fit to all frequency channels within a single sideband, at each time step. This "polyfilter" removes all signals that are common across frequencies, including receiver gain fluctuations, but also contaminating signals that vary smoothly in frequency, such as the atmosphere, CMB, and Galactic foregrounds. This step reduces the noise level by over an order of magnitude and the filtered data are correlated at only a few per cent.
4. A principal component analysis (PCA) identifies signals common across the focal plane and across frequencies then removes the leading modes.
5. Individual frequency channels are flagged if they show evidence of correlations with other frequency channels. We also remove channels where out-of-band signals are aliased.

Calibration in brightness temperature units is then achieved by multiplying the cleaned and coadded TOD by the system temperature measured using the calibration vane.

Data selection is performed on the basis of a variety of statistics that track issues ranging from poor weather conditions to elevations affected by ground pickup (see Foss et al. 2022 for more details). After these cuts have been imposed, we average groups of 16 frequency channels and produce maps for each of these coarser 31.25 MHz-wide channels in order to match the expected width of the observed CO lines (Chung et al. 2019).

Figure 5 shows the cumulative effect of each of the filters described above; the end result is a data set with a very low level of correlated noise without removing significant levels of signal on the scales of interest. Representative maps for each field are shown in Foss et al. (2022).

3.4. CO Power Spectra

The analysis pipeline produces a three-dimensional (3D) map of CO temperature for each field, from which we wish to estimate the "auto-power spectrum," or the variance of the map's Fourier components as a function of spatial frequency. Estimation of this auto-power spectrum for an experiment such as COMAP is challenging. The 3D maps are not uniform in sensitivity and so estimates of the noise power spectrum, which must be subtracted off the measured power spectrum, will be biased by the parts of the maps with the highest noise level. A "pseudo-spectrum" analysis (Hivon et al. 2002) allows us to weight the lower-noise portions of the maps most highly. Even so, the expected level of the CO signal is just a few microkelvin, compared to a typical system temperature of 44 K and contaminating signals of a few millikelvin. To detect such a weak signal reliably, we need a power-spectrum estimation method that is robust in the presence of systematic errors.

The design of the COMAP Pathfinder instrument has some features that naturally lend themselves to such a method. Each of the 19 receiver chains is independent and so a "cross-spectrum" formed from maps computed for different feeds (i.e., the covariance between the Fourier components of the two maps) will be insensitive to systematic errors that are peculiar to any of the individual feeds. The cross-spectrum has the further advantage that the noise contributions of the two different maps do not contribute to its mean and so it directly provides an unbiased estimate of the signal spectrum.

While some systematic errors will be common to all feeds, the cross-spectrum will still be insensitive to such errors as long as the cross-correlation is across not only different feeds but also different subsets of the data that are selected by variables related to these errors. An example of one important systematic error relevant to COMAP is ground pickup. In this case, we can divide the data in two according to scan elevation. We can then ensure that we never form a cross-spectrum using data from the same elevation subset, so that the resulting spectra are as insensitive as possible to this form of contamination. We refer to the power spectrum estimated in this way as the feed–feed pseudo-cross-spectrum (FPXS).

By using only cross-power products from two independent halves of the data, we lose at least a factor of $\sqrt{2}$ in sensitivity compared to the auto-power spectrum. We can, however, approach the auto-power-spectrum sensitivity by splitting the data into many more independent parts and taking the cross-spectra of all possible combinations.

The final pseudo-power cross-spectrum estimate, $\tilde{C}(k)$, is formed by taking the (inverse-variance-weighted) average of all the individual cross-power spectra. Uncertainties in this power spectrum are estimated by assuming (i) that they are dominated by the error bar on the noise power spectrum, and (ii) that the noise is only uncorrelated white noise. We can then create 50 simulated noise maps, where the value in each voxel is drawn from a zero-mean distribution with a standard deviation given by the noise map in that voxel. The standard deviation of the resulting power spectra in each k-bin then gives an estimate of the uncertainty in the signal power spectrum in that bin.

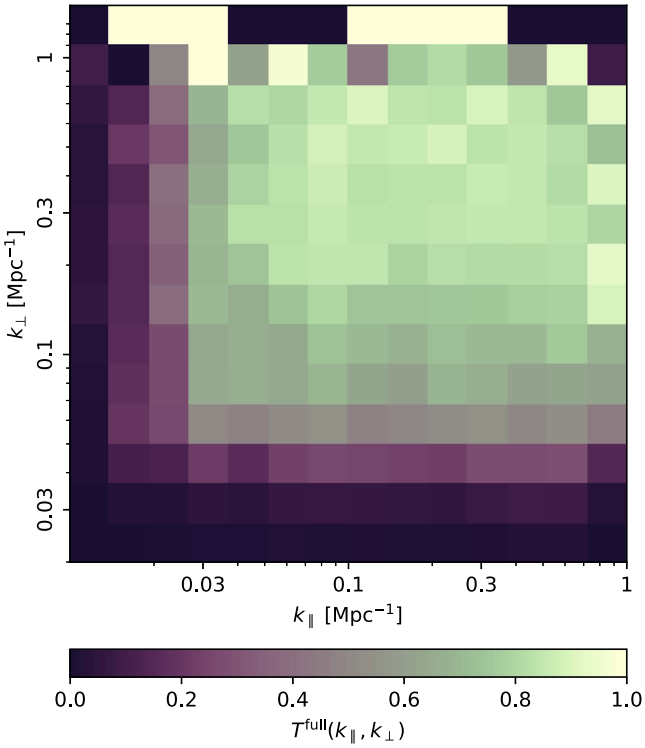

Figure 6. Pipeline transfer function for the cylindrically averaged power spectrum, based on a single signal realization and roughly three hours of data.

The effects on the signal of the instrumental beam and of pipeline filtering, calibration, and map-making are taken into account using transfer functions. The beam transfer function is estimated by comparing the power spectra of mock signal-only maps to those for the maps smoothed with a beam model. We derive the beam model from a physical optics simulation (Lamb et al. 2022), normalized using astrophysical sources to account for the main beam efficiency.

The pipeline transfer function is estimated by combining (noise-dominated) raw data with a simulated signal-only time-ordered data set and processing it through the analysis pipeline in an identical manner to the raw data. Taking the power spectrum of this processed combination and subtracting off that of the raw data, we estimate the transfer function by comparing the result with the power spectrum of the signal-only simulation. We can see that the effect of the pipeline filters (Figure 6) is to suppress sensitivity mostly on the largest scales, both along and perpendicular to the line of sight, while retaining sensitivity on the clustering scales that are of most interest. Because of the instrument's finite angular resolution, the transfer function is very uncertain on the smallest scales perpendicular to the line of sight. However, the beam transfer function ensures that these modes have very low weight (see Foss et al. 2022 for more details).

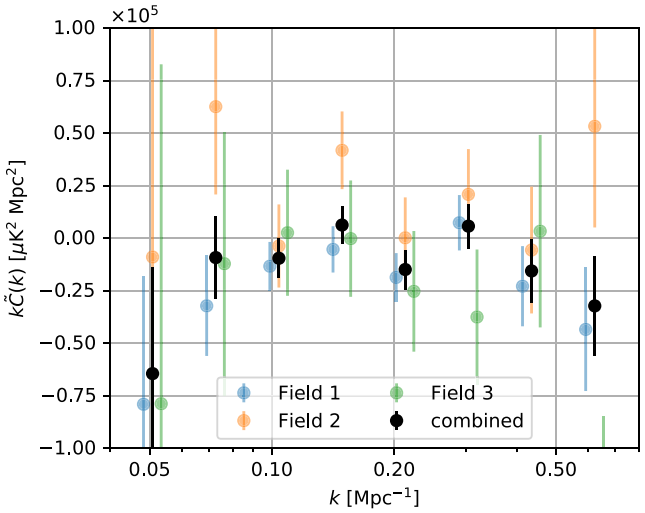

Figure 7. Spherically averaged mean pseudo-cross-spectra for Season 1 observations of Field 1 (blue), Field 2 (orange), and Field 3 (green). These spectra were generated from all the accepted data using the FPXS statistic. In addition, the full transfer function has been applied to debias the signal estimate. Data points from the different fields are offset slightly in k from their actual values to make them easier to distinguish.

With these transfer functions in hand, we produce an unbiased estimate of the signal power spectrum by dividing the pseudo-power cross-spectrum estimate by the full transfer function (combining beam and pipeline effects). Figure 7 shows the final Season 1 power spectra for each field. The spectra for the three fields are combined assuming they are completely uncorrelated, with each k-bin inverse-variance weighted and averaged over the fields. χ^2 statistics for the single-field and combined spectra are given in Ihle et al. (2022). At this stage in the survey, given that our Season 1 observations provide an upper limit and not a detection, we do not perform a full suite of null tests. However, we expect that this will be essential in future analyses in order to exclude possible contributions from a range of potential systematic errors including standing waves and ground pickup.

As a consistency check, we formed cross-spectra between maps of our different fields, split by elevation. Such cross-spectra are sensitive to contributions from systematic errors that are correlated across fields and elevations, whereas the signal of interest should not be present. We find these cross-spectra to be consistent with expectations for white noise (see Ihle et al. 2022 for details). We are working to implement simulations of a range of systematic errors in order to quantify the potential level of contamination to our data, and this work will be the subject of a future publication.

3.5. Expectations for the CO Signal at z ∼ 3

A model for the expected CO signal at $z \sim 3$ was presented by Li et al. (2016) and used to predict the significance of a detection for a COMAP-like experiment. Since then, a number of new observational constraints have become available and we have fielded the Pathfinder, thereby gaining an understanding of the instrument's real-world sensitivity. These developments have provided a motive to update the fiducial model (and also the Pathfinder forecasts, which we discuss in Section 5.1).

The updated model follows the general prescription of Li et al. (2016), using a ladder of relations to assign CO luminosity to halo mass, as follows. A power law is assumed to relate CO ($L'_{\rm CO}$) to infrared ($L_{\rm IR}$) luminosity, which is considered in turn to be proportional to star formation rate (SFR). We connect average SFR to halo mass using empirically constrained "UniverseMachine" (UM) modeling by Behroozi et al. (2019). The combination of these relations has the form of a double power law (motivated from data-driven treatments in Padmanabhan 2017 and Moster et al. 2010) and is a function of their seven individual parameters, some of which are degenerate. In a change to the approach adopted by Li et al. (2016), we therefore simplify the combined relation between CO luminosity, $L'_{\rm CO}$, and halo mass, M_h, to one with four effective free parameters as follows:

$$\frac{L'_{\rm CO}(M_h)}{\rm K\ km\ s^{-1}\ pc^2} = \frac{C}{(M_h/M)^A + (M_h/M)^B} \equiv \frac{C}{m^A + m^B} \quad (1)$$

(see Chung et al. 2022 for expressions relating A, B, C, and M to those of the original scaling relations). To these four parameters, we add σ, which accounts for scatter in the halo/SFR and $L_{\rm IR}/L'_{\rm CO}$ relations. These parameters are uncorrelated in principle, but even in practice we do not expect any correlations that may exist to affect inference of the faint-end slope of the $L(M_h)$ relation, which is the main determinant of the power spectrum on scales to which COMAP is sensitive.

Priors on the values for these parameters were propagated from those on $L_{\rm IR}$–$L'_{\rm CO}$ and $L_{\rm IR}$–SFR used by Li et al. (2016) and the 68% interval around the best-fit values of the other parameters from Behroozi et al. (2019). We also incorporated constraints based on recent observations of CO(1–0) emission from galaxies around $z \sim 3$. These include (i) the CO Luminosity Density at High-z (COLDz; Pavesi et al. 2018; Riechers et al. 2019) survey, a blind molecular line survey of the COSMOS and GOODS-N fields, and (ii) the CO Power Spectrum Survey (COPSS; Keating et al. 2016), a reanalysis of archival Sunyaev–Zel'dovich Array data. Information from these observations is incorporated into our priors by running a Markov Chain Monte Carlo (MCMC) sampler with initial priors on the five parameters, converting halo masses from the Bolshoi–Planck simulation (Behroozi et al. 2019) into CO luminosities and comparing the calculated luminosity functions and shot noise with those based on the observational data. We use the posterior distribution of the model parameters to generate an updated fiducial estimate ("UM+COLDz +COPSS") of the CO power spectrum.

Figure 8 shows our fiducial model along with several others from the literature. It can be seen that our model is somewhat low compared to the constraint from COPSS. This highlights a potential limitation of our approach: its reliance on constraints from a galaxy survey, which can only be sensitive to the brightest objects, means it may omit a significant fraction of the very signal we are searching for. If there is a significant contribution from faint galaxies to the overall average CO luminosity, as hinted by the available LIM constraints (such as those from COPSS), then the fiducial model can only be interpreted as a lower limit.

For this reason, we also consider a model that does not suppress the contribution from faint sources (Keating et al. 2020). Like the fiducial model, this takes the general approach of Li et al. (2016), but uses newer (albeit exclusively local) IR–CO correlation fits from Kamenetzky et al. (2016). The power

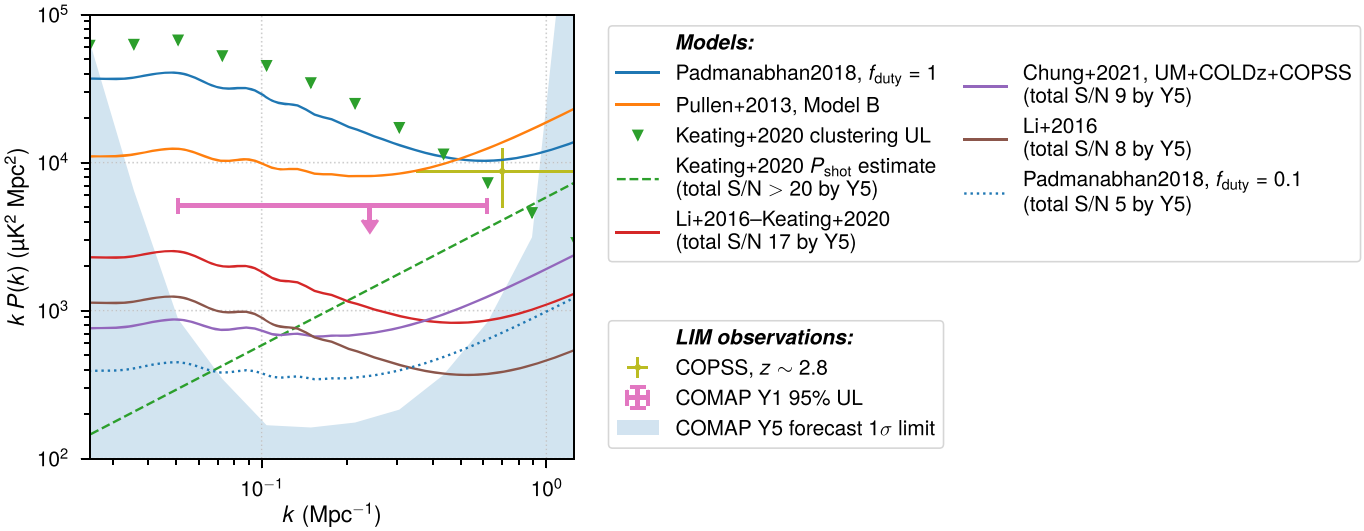

Figure 8. COMAP Pathfinder Season 1 constraint (pink) on the redshift-space CO(1–0) power spectrum at $z \sim 3$, alongside the predictions from various models and our Year 5 Pathfinder sensitivity forecast (blue shaded area). The models include (i) the fiducial COMAP data-driven model from Chung et al. (2022) ("UM+COLDz +COPSS"), (ii) an alternative model from Keating et al. (2020) ("Li+2016–Keating+2020") with emission from faint galaxies that may be missed by the surveys informing the fiducial model, and (iii) models based on $L(M_h)$ relations from Padmanabhan (2017), Pullen et al. (2013), and Li et al. (2016). We also show the COPSS result (Keating et al. 2016) as a direct $P(k)$ measurement and as a constraint on the clustering and shot-noise amplitudes (Keating et al. 2020). For each, the legend indicates the expected signal-to-noise ratio (S/N) with which we would reject the null hypothesis (i.e., excluding sample variance from the calculation).

spectrum for this model is shown in Figure 8, labeled "Li +2016–Keating+2020." For our sensitivity forecasts, discussed in Section 5, we adopt both the UM+COLDz+COPSS and Li+2016–Keating+2020 models in order to represent the range of possible CO signals.

3.6. Constraints from Season 1 Pathfinder Observations

Pipeline, observing, and operational improvements will increase our sensitivity significantly in subsequent observations. However, we already find that Season 1 data alone exclude two models for the power spectrum from the literature and provide the best LIM clustering constraint on CO(1–0) at $z \sim 3$.

From our Season 1 data, we obtain a measurement of $P_{CO}(k) = -2.7 \pm 1.7 \times 10^4\ \mu K^2\,Mpc^3$ on scales $k = 0.051$–$0.62\,Mpc^{-1}$, or a 95% upper limit of $kP_{CO}(k) < 5.1 \times 10^3\ \mu K^2\,Mpc^2$ at $k = 0.24\ Mpc^{-1}$. This is the first direct 3D constraint on the clustering component of the CO(1–0) power spectrum. We plot this constraint in Figure 8 along with that from the COPSS reanalysis of Keating et al. (2020) as well as several models. Our Season 1 upper limit excludes one of the model predictions of Padmanabhan (2017) and Model B of Pullen et al. (2013) at 95% confidence. Being entirely empirical, the former model is driven to a very high clustering amplitude by the incorporation of the COPSS constraint. Its exclusion demonstrates the importance of being able to directly constrain the clustering power spectrum. Exclusion of the latter model has implications for the applicability of the CO–SFR relation used to derive its predictions for CO luminosity at $z \sim 3$.

Our upper limit is not yet sensitive enough to constrain the parameters of our fiducial model but we can use it to set limits on the possible contributions of clustering and shot noise to the total power spectrum, as follows. The observed CO power spectrum, $P_{CO}(k)$, is the sum of clustering and shot-noise terms,

$$P_{CO}(k) = A_{clust}\,P_m(k) + P_{shot}, \quad (2)$$

where A_{clust} is the clustering amplitude, $P_m(k)$ is the dark matter power spectrum, and P_{shot} is the scale-independent shot noise. (These components are shown schematically in Figure 1, right.) Mapping in redshift space imposes distortions on the observed intensity field, such that the clustering amplitude is given by $A_{clust} \approx \langle T \rangle^2 (b^2 + 2b/3 + 1/5)$ for small k, where $\langle T \rangle$ is the mean CO line intensity and b is the luminosity-weighted bias. Our data bounds $A_{clust} < 66\ \mu K^2$, an order-of-magnitude improvement on the Keating et al. (2020) COPSS reanalysis upper limit of $420\ \mu K^2$.

To calculate $P(k)$, we obtain average values of b and v_{eff} (an effective velocity scale used to characterize the effect of line broadening; Chung et al. 2021), from one of our MCMC distributions ("UM + COLDz") and use them to calculate the effect of redshift-space distortions and line broadening. In this way, we obtain the constraints based on COMAP alone shown in Figure 9: $\langle Tb \rangle^2 < 49\ \mu K^2$ and $P_{shot} < 24 \times 10^3\ \mu K^2\ Mpc^3$. Since COMAP is predominantly sensitive to clustering scales, we do not obtain a very tight constraint on the shot-noise component. However, folding in the COPSS result, which is mostly sensitive to shot noise, we obtain only a slightly weaker clustering constraint of $\langle Tb \rangle^2 < 51\ \mu K^2$ and a shot-noise constraint of $P_{shot} = 11.9^{+6.8}_{-6.1} \times 10^3\ \mu K^2\ Mpc^3$. This estimate is much higher than the shot-noise value from the COPSS reanalysis of $5.8^{+3.2}_{-3.5} \times 10^3\ \mu K^2\ Mpc^3$, partly due to accounting for the effect of CO line widths on the observed signal, which may attenuate the COPSS measurement relative to the theoretical comoving shot noise by 40%. Note that since this correction is small relative to the range of model predictions, we do not use it to adjust the COPSS constraint shown in Figure 8 (or used for the derived constraints shown in Figures 10 and 11).

We can obtain a constraint on the H_2 mass density by first adopting a value for b and finding the mean CO temperature $\langle T \rangle$. Conservatively adopting $b > 2$ (which is the case for almost all of the sampled parameter sets for all of our priors and for most models in the literature) and combining this constraint with our limit of $\langle Tb \rangle^2 < 51\ \mu K^2$, we find that $\langle T \rangle < 3.6\ \mu K$. This is the current best LIM-based constraint on CO(1–0) $\langle T \rangle$ at

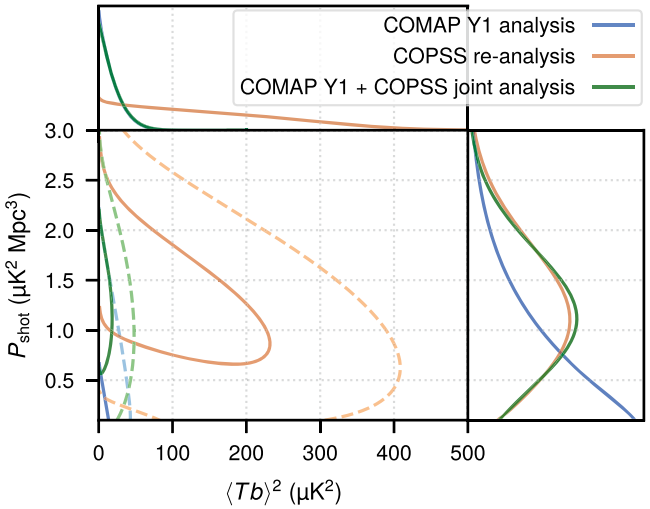

Figure 9. Likelihood contours for the clustering ($\langle Tb\rangle^2$) and shot-noise amplitudes of the CO power spectrum, based on different data sets. The contours represent $\Delta\chi^2 = \{1, 4\}$ relative to the minimum χ^2 obtained in the parameter space, representing 1σ (solid) and 2σ (dashed) for 2D Gaussians. With the COMAP Season 1 data alone, we obtain an order-of-magnitude improvement in the constraint on the clustering amplitude.

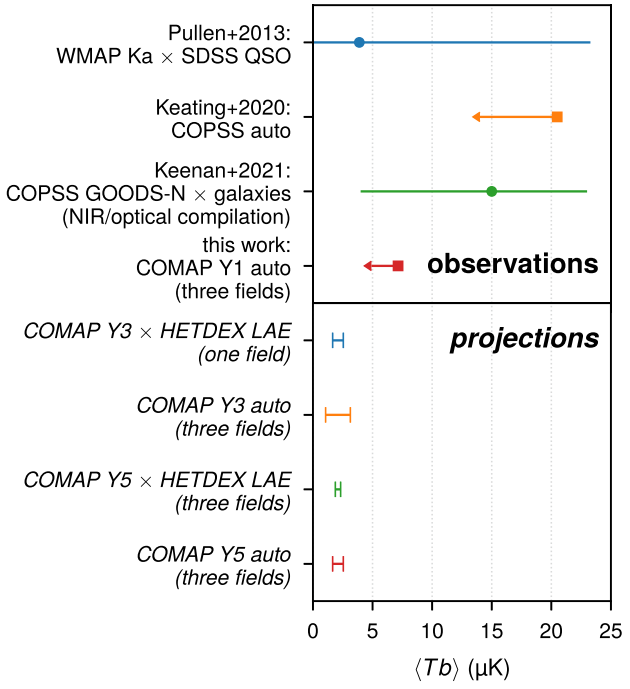

Figure 10. $\langle Tb\rangle$ constraints from previous observational analyses (upper panel), the broadband cross-correlation of Pullen et al. (2013), the auto-power spectrum of Keating et al. (2016), and the 3D cross-correlation of Keenan et al. (2022), alongside our current upper limit, expressed as $\langle Tb\rangle < 7.1\,\mu$K (obtained by assuming $b > 2$). We also show expected future COMAP constraints (lower panel) for both the CO auto-spectrum and CO–galaxy cross-spectrum based on Fisher forecasts described in Chung et al. (2022).

$z \sim 3$; it represents over a factor of 2 improvement compared to $\langle T\rangle < 8.2\,\mu$K derived from the COPSS CO(1–0) auto-spectrum of Keating et al. (2020) and a factor of 3 improvement compared with $\langle T\rangle < 10.9\,\mu$K from the joint COPSS auto- and COPSS–galaxy cross-spectra analysis of Keenan et al. (2022). Since the real-space spectrum (before redshift-space distortions)

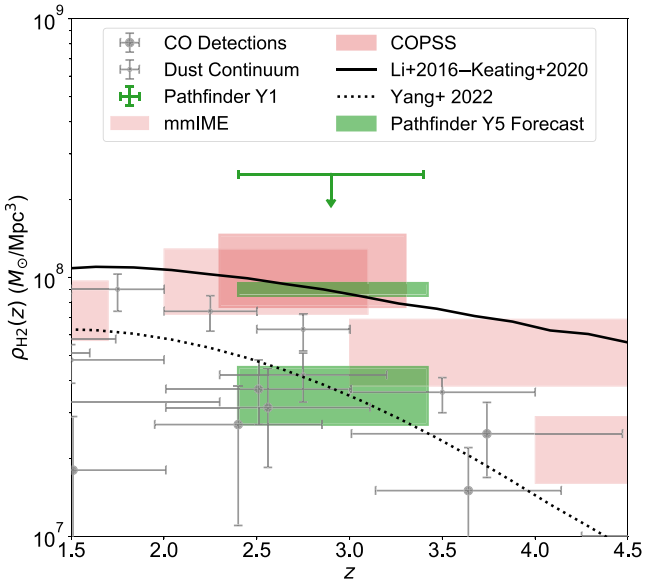

Figure 11. Observational constraints on and models of the cosmic molecular gas density in the redshift range $z = 2$–4. The current COMAP upper limit, and predicted 5 yr constraints (green) for two models (Li+2016–Keating+2020 and UM+COPSS+COLDz) representing the range of possible CO signals, are shown compared with those from galaxy surveys (gray) and intensity-mapping (red) measurements. The molecular gas history inferred from the Li+2016–Keating+2020 model is plotted as a solid line. Since the UM+COPSS+COLDz model does not include a redshift dependence, we show instead (dotted line) the model of Yang et al. (2022) (Yang22), which gives a similar result at $z \sim 3$. In both cases we assume a constant $\alpha_{\rm CO} = 3.6\,M_\odot$ (K km s^{-1} pc^2)$^{-1}$. The galaxy survey points include those compiled by Walter et al. (2020) as well as direct CO observations from ASPECS (Decarli et al. 2020), COLDz (Riechers et al. 2019), and PHIBBS2 (Lenkić et al. 2020). The CO intensity-mapping constraints are from the COPSS (dark red) and mmIME (light red) surveys.

constrains $\langle Tb\rangle$, it is a useful point of comparison between different analyses that may not necessarily take redshift-space distortions into account. In Figure 10 we compare the existing constraints on $\langle Tb\rangle$ and show forecasts for the Pathfinder, including those from a cross-correlation with the HETDEX galaxy survey (to be discussed in Section 5).

Our upper limit on $\langle T\rangle$ can be expressed as a constraint on the H_2 mass density using

$$\rho_{\rm H_2} = \frac{\alpha_{\rm CO}\langle T\rangle H(z)}{(1+z)^2}, \tag{3}$$

where $\alpha_{\rm CO}$ converts between H_2 mass in units of $M_\odot$ and CO luminosity in units of K km s^{-1} pc^2, and $H(z)$ is the Hubble parameter at redshift z. At the central Pathfinder redshift of $z \approx 2.8$, we obtain $\rho_{\rm H_2} < 2.5 \times 10^8\,M_\odot$ Mpc^{-3}, given $\alpha_{\rm CO} = 3.6\,M_\odot$ (K km s^{-1} pc ^{2})$^{-1}$. We show this constraint along with those from other LIM measurements and galaxy surveys in Figure 11. Also plotted are two models representing the range of expected molecular gas density. Unlike constraints from other methods, ours is based on a direct measurement of CO(1–0) at $z \sim 3$ within a large cosmic volume (and so with reduced cosmic variance) and does not make assumptions about CO line ratios. With Season 1 data alone, we obtain a result comparable to that obtained using a >1500 hr integration time on ALMA calibrators (Klitsch et al. 2019), demonstrating the power and scalability of CO LIM.

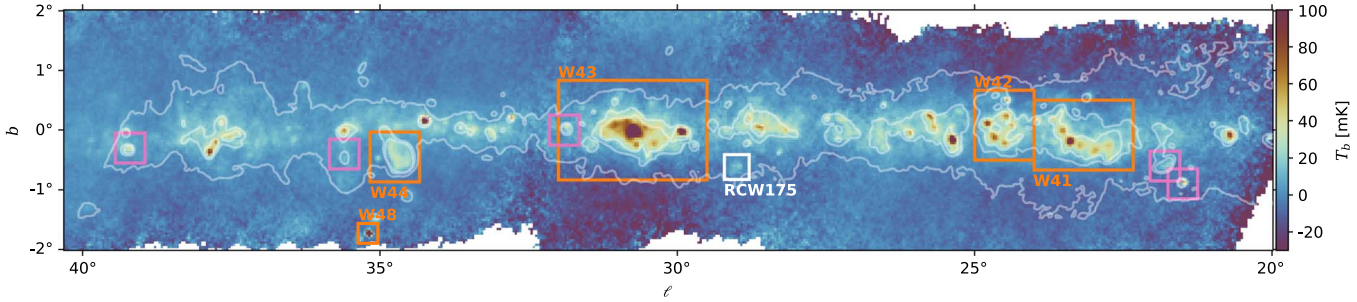

Figure 12. The current COMAP band-averaged 30.5 GHz map covering the Galactic plane between $20° < \ell < 40°$. The color scale is linear and in units of brightness temperature (mK). Contours are 1.0, 1.5, and 2.0 MJy sr^{-1} from the Parkes 5 GHz Galactic plane survey (Calabretta et al. 2014). Typical noise level is 2–3 mK beam^{-1}, equivalently 0.1–0.15 Jy beam^{-1}, away from the edges. Well-known Westerhout star-forming complexes are indicated by orange outlines, including the SNR W44. The other detected SNR are indicated by purple outlines. The RCW175 region, for which a spectral decomposition is shown in Figure 13, is indicated with a white outline. Masked pixels are white.

4. First Results from the COMAP Galactic Plane Survey

Although designed to target LIM measurements of redshifted CO, the Pathfinder instrument also brings new capabilities to bear on the study of line and continuum emission from our own and nearby galaxies. At frequencies around 30 GHz, no other instrument combines the Pathfinder's spatial and spectral resolution with its sensitivity to large angular scales. Observations using the Pathfinder thus fill a gap in existing coverage and have the potential to elucidate the processes of star formation and emission mechanisms of the interstellar medium (ISM), in particular the anomalous microwave emission (AME), which is believed to have its origin in spinning dust grains (Leitch et al. 1997; Dickinson et al. 2018).

During Season 1, around 19 hr per day were spent observing the three LIM science fields and calibrators while the remaining time was available for other targets. We used this time to observe individual compact regions of the Galaxy known to exhibit AME as well as other targets of interest, such as M31. These will be the subject of other papers; here, we present initial results from a survey of the Galactic plane (described in more detail in Rennie et al. 2022).

These results are based on observations using the COMAP Pathfinder only during the period 2019 June to 2021 April, covering Galactic longitudes $20° < \ell < 40°$. Since the end of that period, we have continued to extend the survey along the Galactic plane and the resulting maps (expected to cover $20° < \ell < 220°$) will be the subject of future publications.

Because the observing times for the survey were determined by gaps in availability of the three LIM science fields, it was not possible to observe the survey fields during both rising and setting. For this reason, we found that Lissajous scans (Foss et al. 2022) provided the best cross-linking for map-making. As for the LIM pipeline, data analysis for the Galactic plane survey starts from the raw data as recorded by the instrument, together with pointing information and housekeeping data. After this point, an independent pipeline is used since the LIM pipeline removes any continuum signal.

Initial data selection rejects scans affected by poor weather, identified by examining the feed–feed noise correlation and tracking the $1/f$ noise properties of the data. A running median filter is applied to the TOD to suppress large-scale $1/f$ fluctuations. Ground pickup is removed by fitting a linear slope in azimuth. Calibration is achieved in two steps. First, a relative calibration is performed using the calibration vane; this procedure corrects for atmospheric absorption along the line of sight. Second, absolute calibration to the main beam brightness scale is accomplished using observations of the Crab Nebula (Tau-A) and comparing them to spectral fits from the Wilkinson Microwave Anisotropy Probe.

A destriping map-maker is used to suppress any residual large-scale contamination in the data. This is accomplished by fitting linear offsets to the TOD and making use of scans in different sky orientations to distinguish between the desired sky signal and $1/f$ noise (Delabrouille 1998; Sutton et al. 2009, 2010). This step reduces the $1/f$ noise by at least a factor of 4 on scales up to 30 arcmin.

Figure 12 shows the COMAP 30.5 GHz Galactic plane map, covering $20° < \ell < 40°$. Several bright giant molecular clouds, HII regions, and supernova remnants (SNRs) are detected with high signal-to-noise ratio (S/N). At our observing frequencies, the diffuse emission is dominated by (typically optically thin) free–free emission but there is a significant contribution (20%–40%) from AME (Planck Collaboration et al. 2011, 2015).

By combining the COMAP data with additional surveys at other frequencies, we can decompose the spectral energy distribution (SED) of high-S/N regions into contributions from these two emission mechanisms. We interpret any significant excess over that produced from these two components alone as AME and fit it with a simple lognormal curve that approximates more complete parameterizations (Stevenson 2014).

Using this method, we find six regions within our current map that exhibit significant AME. These are discussed in detail in Rennie et al. (2022), but we show an example of one such SED in Figure 13, for an area containing the bright HII region RCW175 (Rodgers et al. 1960), which has previously been observed to contain AME (see Tibbs et al. 2012; Battistelli et al. 2015). We find that in this region, approximately 50% of the total flux density at 30 GHz is due to AME, consistent with other studies (Dickinson et al. 2009).

We also detect six out of the 33 known SNRs within the currently surveyed area. Our 1 GHz spectral binning of COMAP data allows us to detect evidence of the steeper spectral indices suggesting spectral aging in these sources. Making use of the native spectral resolution of our data, we have also been able to extract five hydrogen radio recombination lines (RRLs) at 20 km s^{-1} velocity resolution. The resulting RRL survey represents the highest-frequency Galactic RRL survey to date.

5. Future Plans for COMAP

This paper has presented the results from the first season of observing with the Pathfinder (approximately 1 yr). We are continuing to observe and expect to achieve a detection of the

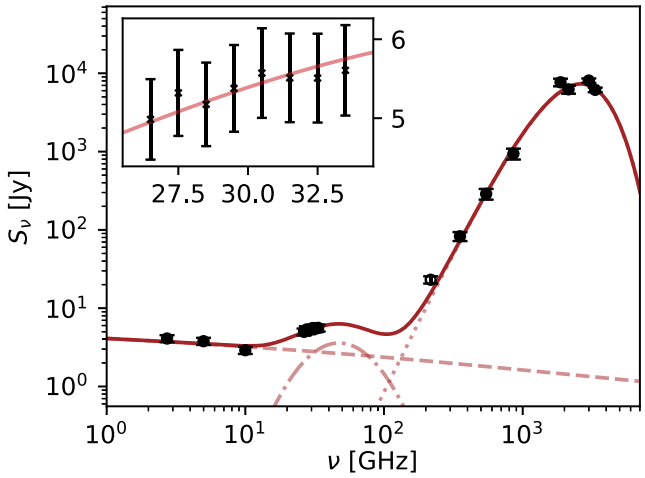

Figure 13. SED for RCW175 featuring COMAP data points between 26 and 34 GHz. Using ancillary data covering 2.7 GHz–3000 GHz (Rennie et al. 2022) we have constrained a three-component model consisting of optically thin free–free emission (dashed line), modified blackbody for thermal emission (dotted line) and spinning dust (dotted–dashed line). The inset panel shows the COMAP band in more detail. The spinning dust component is detected at 4.9σ.

clustering component of the CO auto-power spectrum at $z \sim 3$ within a total of 5 yr of observations and a detection of the CO–galaxy cross-spectrum within a total of 3 yr. We briefly present the forecasts leading to this expectation below (see Chung et al. 2022 for further details).

The CO signal from the end of the EoR also contributes to our Pathfinder data and we expect to be able to place an interesting limit on this through the use of an overlapping Lyα galaxy survey data to mask emission from $z \sim 3$ in the stacked data (Silva et al. 2021). Our ultimate aim, however, is to detect the CO power spectrum from the Epoch of Galaxy Assembly back to the EoR, thereby tracing the global properties of galaxies over cosmic time. The level of the CO signal at such distant epochs is highly uncertain and the subject of continuing investigation. Nevertheless, we examine what current models predict for our prospects to detect such a signal with future phases of the experiment below (see Breysse et al. 2022 for further details).

5.1. Forecasts for the Pathfinder

Our observations thus far have enabled us to develop and demonstrate the understanding and control of systematic errors to the level needed to detect the aggregate CO signal from $z \sim 3$. En route, we have identified and fixed a number of hardware issues (see Lamb et al. 2022). We have also identified a number of remaining issues that can be resolved in the near future, improving the observing efficiency and overall performance (see Foss et al. 2022 for details). Taking these into account and considering the expected performance of the system at the end of 5 yr of observing, we expect a factor of $\sim$69 improvement in sensitivity to the auto-power spectrum compared to that obtained in Season 1. Figure 8 shows the predicted sensitivity compared with the fiducial and other models from the literature.

Even for our conservative fiducial model (which likely underpredicts the contribution from faint sources) we expect a detection of the CO(1–0) auto-power spectrum across all k with S/N of 9 at the end of Year 5. This rises to S/N of 17 if we consider the Li+2016–Keating+2020 model, which predicts a greater contribution from faint sources. For the fiducial model, Figure 10 (lower panel) shows the projected constraints on $\langle Tb \rangle$. After 3 yr of observing with the Pathfinder, we expect a marginal 2σ null rejection of $\langle Tb \rangle = 2.1 \pm 1.0\ \mu$ K, but this will improve to a $\approx 5\sigma$ constraint after 5 yr. For the Li+2016–Keating+2020 model, the higher expected $P(k)$ S/N would yield correspondingly tighter constraints on $\langle Tb \rangle$, with significances of 6σ after 3 yr and 12σ after 5 yr. We obtain similar constraints on the molecular gas density, ρ_{H_2}, predicted from these two models (Figure 11).

In addition to their potential to detect the CO(1–0) auto-power spectrum, the Pathfinder observations were designed to overlap with the volume covered by HETDEX, a spectroscopic galaxy survey, allowing a CO–galaxy cross-correlation. Chung et al. (2019) found that the expected S/N for this cross-spectrum would be significantly greater than that expected for the CO auto-spectrum. In an updated forecast based on the UM +COLDz+COPSS model, Chung et al. (2022) find that, based on very conservative assumptions, we expect to detect the cross-spectrum over all k with a S/N of 7 after 3 yr using Field 1 data alone, rising to 19 after 5 yr using data across all three fields. In terms of a constraint on $\langle Tb \rangle$, this corresponds to a 5σ detection after 3 yr (one field), rising to 10σ at the end of the 5 yr period (three fields; see Figure 10). Again, these constraints would be significantly tighter for the Li+2016–Keating+2020 model, at 8σ and 13σ after 3 yr (one field) and 5 yr (three fields), respectively.

We note that the large volume covered by COMAP enables multiple voxel-level analyses that will allow us to explore the CO signal in more detail. Ihle et al. (2019) showed that we can use the one-point voxel intensity distribution (VID; Breysse et al. 2017) to improve our measurement of the CO luminosity function beyond what is possible with the power spectrum alone (see also discussion in Chung et al. 2022). The availability of the overlapping HETDEX catalog enables several other analyses (Silva et al. 2021; Breysse et al. 2019). Stacking COMAP voxels containing HETDEX galaxies is expected to result in a detection of the total CO signal with S/N 2–3 times higher than that obtained using all COMAP voxels. New "conditional VID" measurements examining the intensity distribution within the stacked voxels can be used to further break down the CO luminosity function and how it changes in HETDEX sources. A constraint on the CO(2–1) emission from $z \sim 6$ may be obtained by using the HETDEX catalog to mask COMAP voxels containing signal from $z \sim 3$. With the high S/N expected for the total stacked CO signal at $z \sim 3$, it will be possible to examine the variation of the CO signal and the CO–galaxy cross-spectrum with spatial scale and their evolution with redshift at the peak of cosmic star formation.

5.2. Prospects for *COMAP*-EoR

In order to target the signal from the EoR, we envisage an enhanced instrument, COMAP-*EoR*, consisting of the existing 30 GHz Pathfinder plus two duplicate receivers mounted on two more 10.4 m telescopes, as well as a 19-feed 16 GHz receiver mounted on a prototype ngVLA 18 m dish. The 10.4 m dishes are already available for this use at OVRO and the ngVLA dish will be dedicated to COMAP in 2026. The main features of the 30 GHz instruments are shown in Table 2 and those of the 16 GHz receiver are listed in Table 4. For the latter, the system temperature is expected to be significantly lower

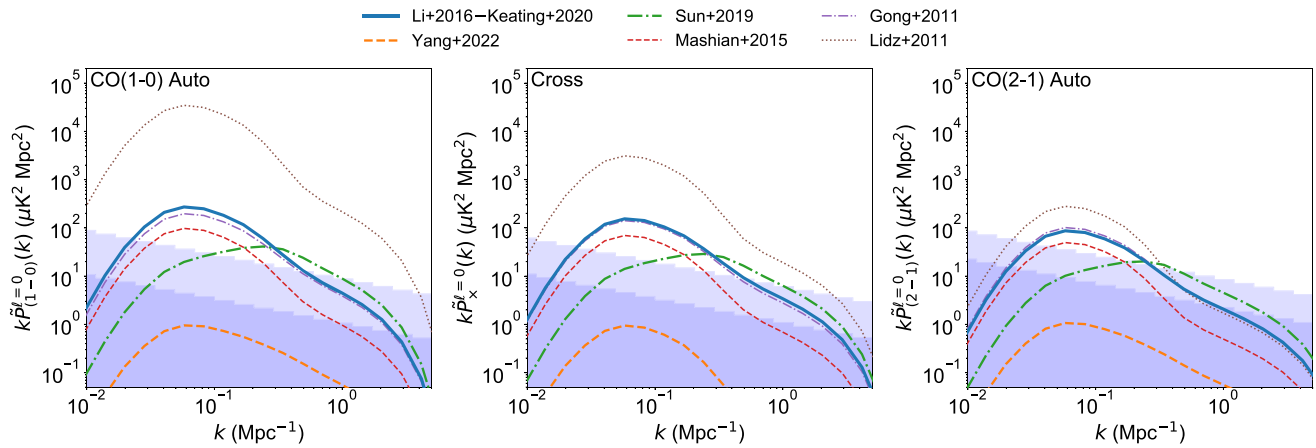

Figure 14. Forecast 1σ COMAP-*EoR* and COMAP-*ERA* sensitivities (light and dark shaded bands, respectively) at $z = 6.2$ for models from Lidz et al. (2011; brown dotted), Gong et al. (2012; purple dotted–dashed), Mashian et al. (2015; red dashed), and Sun et al. (2019; green dotted–dashed), as well as the Li+2016–Keating +2020 and Yang22 models from Figure 11. Predictions are shown for the CO(1–0) auto-spectra (left), the CO(1–0)–CO(2–1) cross-spectra (center), and the CO(2–1) auto-spectra (right).

Table 4
COMAP-*EoR* Instrument Parameters

Parameter	Value
Primary reflector diameter	18 m
No. of feeds	19
Polarization	Dual
Beam FWHM @ 16 GHz	3.7′
System temperature	20–27 K
Frequency resolution (native)	∼2 MHz
Frequency bands	Redshift coverage
Band 1: 12–13 GHz	7.8–8.6
Band 2: 13–15 GHz	6.7–7.8
Band 3: 15–17 GHz	5.8–6.7
Band 4: 17–20 GHz	4.8–5.8

Table 5
Predicted S/N Obtained by COMAP-*EoR* and COMAP-*ERA* in each of the Instruments' Bands (as defined in Table 4), along with the Combined Total (Assuming the Four Frequency Bins are Independent)

	Band 1	2	3	4	
Redshift	7.8–8.6	6.7–7.8	5.8–6.7	4.8–5.8	Total
Li16/Keating20	2.2/13	9/39	15/60	21/89	28/114
Yang22	0.0/0.0	0.0/0.1	0.1/0.8	0.6/4.3	0.6/4.4
Sun19	0.2/2.0	2.7/18	11/66	22/143	25/159
Mashian15	0.2/1.2	1.9/11	7.2/29	16/60	18/68
Gong11	0.3/2.4	3.7/20	13/53	30/115	33/128
Lidz11	52/126	114/290	179/456	357/811	418/983

Note. Each entry shows the S/Ns for both COMAP-*EoR* and COMAP-*ERA*, separated by a slash. The column for Band 3 corresponds to the redshift range for the model predictions of Figure 14.

than for the existing 30 GHz instrument due to a combination of lower spillover, low-noise amplifier noise temperature, and atmospheric contributions. The extra 30 GHz systems will provide more sensitivity to CO(2–1) at $z = 6$–8 and CO(1–0) at $z = 2.4$–3.4, while the 16 GHz system will open a new window on CO(1–0) at $z = 4.8$–8.6 (see Figure 2).

For the purposes of these forecasts, we assume that the 16 GHz receiver will begin observing at the conclusion of the 5 yr Pathfinder survey and the two new 30 GHz receivers two years after that. After five years of observations with all four instruments, we will have obtained 12 years on the Pathfinder, seven years with the 16 GHz receiver, and five years with each of the new 30 GHz receivers. This will provide 29,000 dish-hours/field at 30 GHz (accounting for the $T_{\rm sys}$ adjustment) and 7000 dish-hours/field at 16 GHz. We also consider an "expanded reionization array" (ERA) concept where the number of dishes is increased to a total of 10 at both frequencies, observing for a further five years to produce 110,000 dish-hours at 30 GHz and 57,000 dish-hours at 16 GHz.

Figure 14 shows the predicted sensitivity at $z = 6.2$ for COMAP-*EoR* and COMAP-*ERA* with respect to a number of models for the power-spectrum monopole from the literature, including Li+2016–Keating+2020 (which was also adopted for our $z \sim 3$ forecasts in Section 5.1). Overall, the models span four orders of magnitude in the amplitude of the power spectrum, highlighting our deep ignorance of the processes giving rise to the emission at this redshift and, consequently, the amount that can be learned through observations of this type.

Table 5 shows the S/Ns expected in each of the four COMAP-*EoR* bands as well as the total (combining detection significances from the monopole, quadrupole, and hexadecapole measurements). For all models except the most pessimistic (Yang22), we detect the signal from the EoR at high significance for the COMAP-*EoR* survey and can also resolve the redshift evolution of the signal over the full $z = 4.8$–8.6 range. COMAP-*ERA* produces even higher detection significances for the same three fields, although in practice our observing strategy would likely alter to cover wider areas for cross-correlation with other LIM experiments including those targeting H I.

Assuming a linear relationship between the CO emission and molecular gas abundance (i.e., Equation (3)), we can forecast the constraints imposed on the latter by our measurement of the CO power spectrum. As well as the Li+2016–Keating+2020 model, we also consider the most pessimistic, Yang22. The former is consistent with constraints from LIM measurements while the latter is even more pessimistic than constraints from galaxy surveys would suggest.

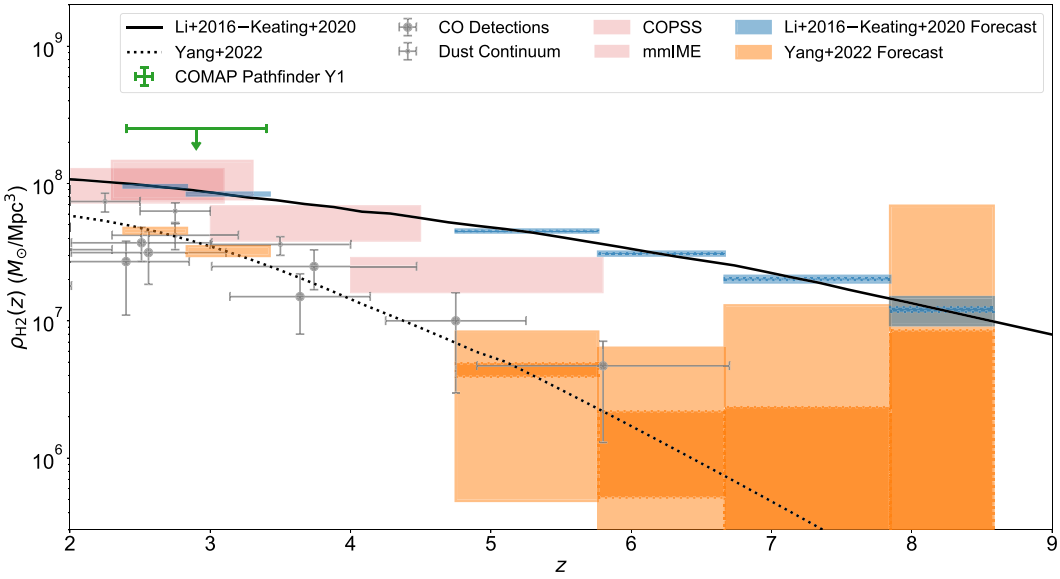

Figure 15. Predicted COMAP constraints on the cosmic molecular gas history compared with existing direct and intensity-mapping measurements at redshifts covered by future phases of COMAP. The plotted models, data, and constraints are as in Figure 11. Blue and orange boxes show the 95% constraints obtained on these models using COMAP-*EoR* (light) and COMAP-*ERA* (dark). For reference, we also show the COMAP Y1 constraint from Figure 11.

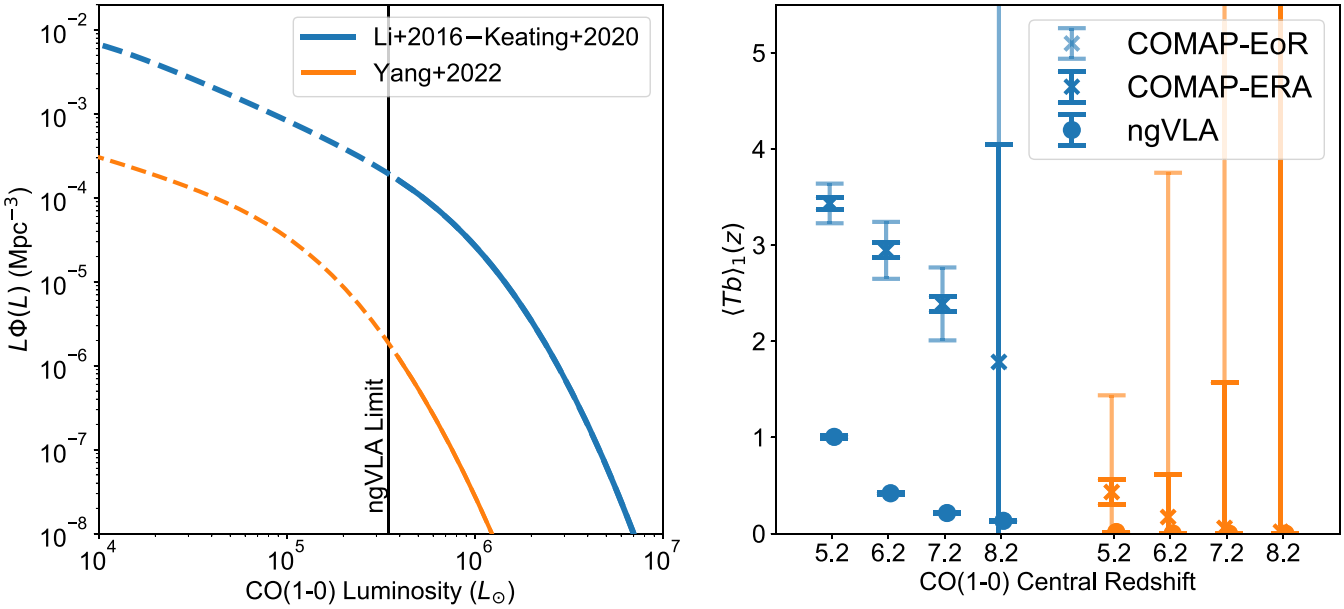

Figure 16. Left: CO(1–0) luminosity functions at $z = 6.2$ of the Li+2016–Keating+2020 (blue) and Yang22 (orange) models, with the limit of a hypothetical ngVLA molecular gas survey marked in black. Dashed lines show the portions of the luminosity functions that are directly accessible only to a LIM survey. Right: uncertainties on the CO(1–0) power-spectrum amplitude factor for the same two models. Circles show measurements that would be obtained by an ngVLA-like survey, ×'s show our forecasts for COMAP-*EoR* (light) and COMAP-*ERA* (dark).

These models and the predicted constraints for COMAP-*EoR* and COMAP-*ERA* are shown in Figure 15, along with existing constraints from galaxy surveys and LIM measurements. COMAP-*EoR* allows us to place very tight constraints on the cosmic molecular gas density in the case where, as suggested by existing LIM measurements, there is a significant contribution from faint galaxies that are missed by current galaxy surveys. For the most pessimistic model, COMAP-*ERA* is needed to constrain the molecular gas abundance at high redshift.

The ability of LIM to distinguish between these two cases is a key driver for these observations. Figure 16 (left) shows the luminosity functions for our two demonstration models and the detection limit of a hypothetical ngVLA CO(1–0) survey of a deep field as described in Decarli et al. (2018). Galaxies below this limit can be directly detected in aggregate by a LIM measurement. The clustering amplitude inferred from the ngVLA survey (for each model) is shown in Figure 16 (left) compared with projected constraints from COMAP-*EoR* and COMAP-*ERA*. For the Li+2016–Keating+2020 model, the value derived from the ngVLA survey underestimates the clustering amplitude by a large factor. Even if the true high-redshift signal resembles the most pessimistic model (Yang22),

LIM observations like COMAP are still required to constrain the possible contribution from faint galaxies.

6. Conclusions

The field of LIM holds the promise of characterizing the global properties of galaxies over huge spatial volumes across cosmic time. CO has many advantages as a tracer of galaxies for this purpose and provides a measurement that is complementary to galaxy surveys and redshifted 21 cm. A necessary first step on this path is the validation of the technologies as well as the observational and analytical strategies required to detect the CO signal at intermediate redshifts; this has now been accomplished.

We have constructed and fielded a CO LIM Pathfinder and have begun a 5 yr survey of redshifted CO(1–0) emission from galaxies at $z = 2.4$–3.4. Using data from our first ∼13 months, we have demonstrated the ability of the instrument and our first-generation analysis pipeline to produce data with the required low levels of correlated noise.

From our Season 1 data, we obtain a measurement of $P_{\rm CO}(k) = -2.7 \pm 1.7 \times 10^4\ \mu{\rm K}^2\,{\rm Mpc}^3$ on scales $k = 0.051$–$0.62\,{\rm Mpc}^{-1}$, or a 95% upper limit of $kP_{\rm CO}(k) < 5.1 \times 10^3\,\mu{\rm K}^2\,{\rm Mpc}^2$ at $k = 0.24\ {\rm Mpc}^{-1}$. This is the first direct 3D constraint on the clustering component of the CO(1–0) power spectrum.

This constraint on the auto-power spectrum excludes two models from the literature and resolves ambiguities in the interpretation of the COPSS shot-noise measurement.

We use this measurement to determine a constraint on the amplitude of the clustering power spectrum, $\langle Tb\rangle^2 < 49\ \mu{\rm K}^2$, nearly an order-of-magnitude improvement on the previous best constraint from COPSS. In a reanalysis of the COPSS measurement in tandem with COMAP data, we also obtain a shot-noise power, $P_{\rm shot} = 1.2^{+0.7}_{-0.6} \times 10^4\ \mu{\rm K}^2\ {\rm Mpc}^3$, suggesting that the constraint from COPSS alone of $5.8^{+3.2}_{-3.5} \times 10^3\ \mu{\rm K}^2\ {\rm Mpc}^3$ was underestimated due to line broadening as well as less stringent clustering amplitude constraints.

In addition to pursuing its primary CO LIM science goals, the Pathfinder is also conducting a 30 GHz survey of the Galactic plane, to cover Galactic longitudes $\ell \sim 20°$–$200°$ and Galactic latitudes $|b| < 1.^\circ5$, with an angular resolution of $4.'5$. We have presented preliminary maps of the plane covering $20° < \ell < 40°$, demonstrating the ability of the Pathfinder to perform continuum mapping as well as its primary science of spectroscopy. These observations fill a gap in spatial and spectral resolution of the Galactic plane at these frequencies. Performing a spectroscopic decomposition of the emission for point sources in our preliminary map, we find evidence of anomalous microwave emission in a number of these sources. We also detect radio recombination lines at high significance, which will provide a useful resource for the community.

Using the performance of the instrument and analysis pipeline during this first season as a guide and taking into account a range of improvements both already implemented and expected, we forecast the expected constraints on the CO auto-spectrum at the end of a nominal 5 yr observing campaign. For the auto-power spectrum, we predict a detection with total S/N of 9–17 after 5 yr. For the cross-power spectrum with an overlapping galaxy survey, we predict a S/N of 7 after 3 yr from just one field, rising to 19 after 5 yr coadding data across all three COMAP fields.

The availability of an overlapping galaxy catalog also permits various stacking analyses involving selection of COMAP voxels based on their galaxy content, resulting in increased S/N on the stacked CO signal by factors of 2–3 compared to that obtained stacking all COMAP voxels. Similarly, masking COMAP voxels based on their $z \sim 3$ galaxy content allows us to place a 6σ limit on the contribution of CO(2–1) from $z \sim 6$.

Looking further ahead, we envisage an enhanced experiment, COMAP-*EoR*, targeting the EoR directly by adding more pixels at 30 GHz as well as a new 16 GHz receiver (on a prototype ngVLA antenna due to be dedicated to COMAP in 2026). Current models for the CO signal at $z \sim 6$ span four orders of magnitude, indicating the potential for experimental constraints to improve our understanding of galaxies and the ISM at this epoch. We presented a survey design that provides for a detection at high significance for our fiducial $z \sim 6$ model. The resulting constraints on molecular gas abundance have the potential to directly detect or rule out a contribution from faint galaxies that would otherwise be missed by galaxy surveys conducted by future facilities such as the ngVLA.

We also describe a much more powerful experiment, COMAP-*ERA*, with more feeds at 30 and 16 GHz, capable of making a 100σ detection of the EoR CO signal. This could enable a cross-correlation of CO from the ionized ISM of galaxies with 21 cm observations of the neutral IGM, to provide constraints on the evolution of ionized regions during reionization (Lidz et al. 2011).

This material is based upon work supported by the National Science Foundation under grant Nos. 1517108, 1517288, 1517598, 1518282, and 1910999, and by the Keck Institute for Space Studies under "The First Billion Years: A Technical Development Program for Spectral Line Observations." Parts of the work were carried out at the Jet Propulsion Laboratory, California Institute of Technology, under a contract with the National Aeronautics and Space Administration, and funded through the internal Research and Technology Development program. DTC is supported by a CITA/Dunlap Institute postdoctoral fellowship. The Dunlap Institute is funded through an endowment established by the David Dunlap family and the University of Toronto. C.D. and S.H. acknowledge support from an STFC Consolidated grant (ST/P000649/1). J.B., H.K. E., M.K.F., H.T.I., J.G.S.L., M.R., N.O.S., D.W., and I.K.W. acknowledge support from the Research Council of Norway through grant Nos. 251328 and 274990, and from the European Research Council (ERC) under the Horizon 2020 Research and Innovation Program (grant agreement No. 819478, COSMOGLOBE). J.G. acknowledges support from the University of Miami and is grateful to Hugh Medrano for assistance with cryostat design. L.K. was supported by the European Unions Horizon 2020 research and innovation program under the Marie Skodowska-Curie grant agreement No. 885990. J.K. is supported by a Robert A. Millikan Fellowship from Caltech. At JPL, we are grateful to Mary Soria for assembly work on the amplifier modules and to Jose Velasco, Ezra Long, and Jim Bowen for the use of their amplifier test facilities. H.P. acknowledges support from the Swiss National Science Foundation through Ambizione Grant PZ00P2_179934. P.C. B. is supported by the James Arthur Postdoctoral Fellowship. R.R. acknowledges support from ANID-FONDECYT grant No. 1181620. L.B. was supported by ANID-PFCHA/DOCTORADO NACIONAL 2019-21192138. M.V. acknowledges support from the Kavli Institute for Particle Astrophysics and Cosmology. We thank Isu Ravi for her contributions to the

warm electronics and antenna drive characterization. Finally, we thank the anonymous referee, whose comments and suggestions have helped to improve and clarify this manuscript.

ORCID iDs

Kieran A. Cleary https://orcid.org/0000-0002-8214-8265
Patrick C. Breysse https://orcid.org/0000-0001-8382-5275
Dongwoo T. Chung https://orcid.org/0000-0003-2618-6504
Hans Kristian Eriksen https://orcid.org/0000-0003-2332-5281
Marie Kristine Foss https://orcid.org/0000-0001-8896-3159
Stuart E. Harper https://orcid.org/0000-0001-7911-5553
Andrew I. Harris https://orcid.org/0000-0001-6159-9174
Håvard T. Ihle https://orcid.org/0000-0003-3420-7766
Junhan Kim https://orcid.org/0000-0002-4274-9373
James W. Lamb https://orcid.org/0000-0002-5959-1285
Hamsa Padmanabhan https://orcid.org/0000-0002-8800-5740
Timothy J. Pearson https://orcid.org/0000-0001-5213-6231
Liju Philip https://orcid.org/0000-0001-7612-2379
Anthony C. S. Readhead https://orcid.org/0000-0001-9152-961X
Thomas J. Rennie https://orcid.org/0000-0002-1667-3897
Marta B. Silva https://orcid.org/0000-0003-0209-4816
Nils-Ole Stutzer https://orcid.org/0000-0001-5301-1377
Bade D. Uzgil https://orcid.org/0000-0001-8526-3464
Duncan J. Watts https://orcid.org/0000-0002-5437-6121
Ingunn Kathrine Wehus https://orcid.org/0000-0003-3821-7275
J. Richard Bond https://orcid.org/0000-0003-2358-9949
Delaney A. Dunne https://orcid.org/0000-0002-5223-8315
Brandon Hensley https://orcid.org/0000-0001-7449-4638
Laura C. Keating https://orcid.org/0000-0001-5211-1958
Roberta Paladini https://orcid.org/0000-0002-5158-243X
Rodrigo Reeves https://orcid.org/0000-0001-5704-271X
Marco P. Viero https://orcid.org/0000-0003-0545-4872
Risa H. Wechsler https://orcid.org/0000-0003-2229-011X

References

Akeson, R., Armus, L., Bachelet, E., et al. 2019, arXiv:1902.05569
Bandura, K., Addison, G. E., Amiri, M., et al. 2014, Proc. SPIE, 9145, 914522
Battistelli, E. S., Carretti, E., Cruciani, A., et al. 2015, ApJ, 801, 111
Behroozi, P., Wechsler, R. H., Hearin, A. P., & Conroy, C. 2019, MNRAS, 488, 3143
Breysse, P. C., Anderson, C. J., & Berger, P. 2019, PhRvL, 123, 231105
Breysse, P. C., Chung, D. T., Cleary, K. A., et al. 2022, ApJ, 933, 188
Breysse, P. C., Kovetz, E. D., Behroozi, P. S., Dai, L., & Kamionkowski, M. 2017, MNRAS, 467, 2996
Breysse, P. C., Kovetz, E. D., & Kamionkowski, M. 2014, MNRAS, 443, 3506
Brown, R. L., & Vanden Bout, P. A. 1991, AJ, 102, 1956
Calabretta, M. R., Staveley-Smith, L., & Barnes, D. G. 2014, PASA, 31, e007
Carilli, C. L., & Walter, F. 2013, ARA&A, 51, 105
Cataldo, G., Ade, P., Anderson, C., et al. 2021, arXiv:2101.11734
CCAT-Prime Collaboration, Aravena, M., Austermann, J. E., et al. 2021, arXiv:2107.10364
Chung, D. T., Breysse, P. C., Cleary, K. A., et al. 2022, ApJ, 933, 186
Chung, D. T., Breysse, P. C., Tveit Ihle, H., et al. 2021, ApJ, 923, 188
Chung, D. T., Viero, M. P., Church, S. E., et al. 2019, ApJ, 872, 186
Crites, A. T., Bock, J. J., Bradford, C. M., et al. 2014, Proc. SPIE, 9153, 91531W
DeBoer, D. R., Parsons, A. R., Aguirre, J. E., et al. 2017, PASP, 129, 045001
Decarli, R., Aravena, M., Boogaard, L., et al. 2020, ApJ, 902, 110
Decarli, R., Carilli, C., Casey, C., et al. 2018, in ASP Conf. Ser. 517, Science with a Next Generation Very Large Array, ed. E. Murphy (San Francisco, CA: ASP), 565
Delabrouille, J. 1998, A&AS, 127, 555
Dickinson, C., Ali-Haïmoud, Y., Barr, A., et al. 2018, NewAR, 80, 1
Dickinson, C., Davies, R. D., Allison, J. R., et al. 2009, ApJ, 690, 1585
Finkelstein, S. L., Dickinson, M., Ferguson, H. C., et al. 2017, The Cosmic Evolution Early Release Science (CEERS) Survey, JWST Proposal ID 1345. Cycle 0 Early Release Science
Foss, M. K., Ihle, H. T., Borowska, J., et al. 2022, ApJ, 933, 184
Gebhardt, K., Mentuch Cooper, E., Ciardullo, R., et al. 2021, ApJ, 923, 217
Gong, Y., Cooray, A., Silva, M., et al. 2012, ApJ, 745, 49
Hill, G. J., Gebhardt, K., Komatsu, E., et al. 2008, in ASP Conf. Ser. 399, Panoramic Views of Galaxy Formation and Evolution, ed. T. Kodama, T. Yamada, & K. Aoki (San Francisco, CA: ASP), 115
Hill, G. J., Lee, H., MacQueen, P. J., et al. 2021, ApJ, 162, 298
Hivon, E., Górski, K. M., Netterfield, C. B., et al. 2002, ApJ, 567, 2
Ihle, H. T., Borowska, J., Cleary, K. A., et al. 2022, ApJ, 933, 185
Ihle, H. T., Chung, D., Stein, G., et al. 2019, ApJ, 871, 75
Kamenetzky, J., Rangwala, N., Glenn, J., Maloney, P. R., & Conley, A. 2016, ApJ, 829, 93
Keating, G. K., Marrone, D. P., Bower, G. C., & Keenan, R. P. 2020, ApJ, 901, 141
Keating, G. K., Marrone, D. P., Bower, G. C., et al. 2016, ApJ, 830, 34
Keenan, R. P., Keating, G. K., & Marrone, D. P. 2022, ApJ, 927, 161
Klitsch, A., Péroux, C., Zwaan, M. A., et al. 2019, MNRAS, 490, 1220
Koekemoer, A., Foley, R. J., Spergel, D. N., et al. 2019, BAAS, 51, 550
Korngut, P. M., Bock, J. J., Akeson, R., et al. 2018, Proc. SPIE, 10698, 106981U
Kovetz, E. D., Viero, M. P., Lidz, A., et al. 2017, arXiv:1709.09066
Lagache, G. 2018, in IAU Symp. 333, Peering towards Cosmic Dawn, ed. V. Jelic & T. van der Hulst (Cambridge: Cambridge Univ. Press), 228
Lamb, J. W., Cleary, K. A., Woody, D. P., et al. 2022, ApJ, 933, 183
Leighton, R. B. 1977, Final Technical Report for National Science Foundation Project AST 73-04708, California Institute of Technology, https://resolver.caltech.edu/CaltechAUTHORS:20121023-144727561
Leitch, E. M., Readhead, A. C. S., Pearson, T. J., & Myers, S. T. 1997, ApJL, 486, L23
Lenkić, L., Bolatto, A. D., Förster Schreiber, N. M., et al. 2020, AJ, 159, 190
Li, T. Y., Wechsler, R. H., Devaraj, K., & Church, S. E. 2016, ApJ, 817, 169
Lidz, A., Furlanetto, S. R., Oh, S. P., et al. 2011, ApJ, 741, 70
Mashian, N., Sternberg, A., & Loeb, A. 2015, JCAP, 2015, 028
Moster, B. P., Somerville, R. S., Maulbetsch, C., et al. 2010, ApJ, 710, 903
Newburgh, L. B., Bandura, K., Bucher, M. A., et al. 2016, Proc. SPIE, 9906, 99065X
Padmanabhan, H. 2017, MNRAS, 475, 1477
Parsons, A., Backer, D., Chang, C., et al. 2006, in 2006 Fortieth Asilomar Conf. on Signals, Systems and Computers (Piscataway, NJ: IEEE), 2031
Pavesi, R., Sharon, C. E., Riechers, D. A., et al. 2018, ApJ, 864, 49
Planck Collaboration, Abergel, A., Ade, P. A. R., et al. 2011, A&A, 536, A21
Planck Collaboration, Ade, P. A. R., Aghanim, N., et al. 2015, A&A, 580, A13
Planck Collaboration, Aghanim, N., Akrami, Y., et al. 2020, A&A, 641, A1
Pullen, A. R., Chang, T.-C., Doré, O., & Lidz, A. 2013, ApJ, 768, 15
Rennie, T. J., Harper, S. E., Dickinson, C., et al. 2022, ApJ, 933, 187
Riechers, D. A., Pavesi, R., Sharon, C. E., et al. 2019, ApJ, 872, 7
Rodgers, A. W., Campbell, C. T., & Whiteoak, J. B. 1960, MNRAS, 121, 103
Santos, M., Bull, P., Alonso, D., et al. 2015, in Proc. of Science 215, Advancing Astrophysics with the Square Kilometre Array (AASKA14) (Trieste: SISSA), 019
Silva, M. B., Baumschlager, B., Cleary, K. A., et al. 2021, arXiv:2111.05354
Stevenson, M. A. 2014, ApJ, 781, 113
Sun, G., Hensley, B. S., Chang, T.-C., Doré, O., & Serra, P. 2019, ApJ, 887, 142
Sutton, D., Johnson, B. R., Brown, M. L., et al. 2009, MNRAS, 393, 894
Sutton, D., Zuntz, J. A., Ferreira, P. G., et al. 2010, MNRAS, 407, 1387
Tibbs, C. T., Paladini, R., Compiègne, M., et al. 2012, ApJ, 754, 94
Vieira, J., Aguirre, J., Bradford, C. M., et al. 2020, arXiv:2009.14340
Walter, F., Carilli, C., Decarli, R., et al. 2019, BAAS, 51, 442
Walter, F., Carilli, C., Neeleman, M., et al. 2020, ApJ, 902, 111
Yang, S., Popping, G., Somerville, R. S., et al. 2022, ApJ, 929, 140